

Evaluating the effect of using different reference spectra on SAM classification results: an implication for hydrothermal alteration mapping

M. Honarmand^{1*}, H. Ranjbar², H. Shahriari³ and F. Naseri¹

1. Department of Ecology, Institute of Science and High Technology and Environmental Sciences, Graduate University of Advanced Technology, Kerman, Iran

2. Department of Mining Engineering, Shahid Bahonar University of Kerman, Kerman, Iran

3. Department of Mining Engineering, Vali-e-Asr University of Rafsanjan, Rafsanjan, Iran

Received 11 May 2018; received in revised form 12 June 2018; accepted 19 June 2018

*Corresponding author: mehonarmand167@yahoo.com (M. Honarmand).

Abstract

This research was performed with the objective of evaluating the accuracy of spectral angle mapper (SAM) classification using different reference spectra. The Advanced Spaceborne Thermal Emission and Reflection Radiometer (ASTER) digital images were applied in the SAM classification in order to map the distribution of hydrothermally altered rocks in the Kerman Cenozoic magmatic arc (KCMA), Iran. The study area comprises main porphyry copper deposits such as Meiduk and Chahfiroozeh. Collecting reference spectra was considered after pre-processing of ASTER VNIR/SWIR images. Three types of reference spectra including image, USGS library, and field samples spectra were used in the SAM algorithm. Ground truthing and laboratory studies including thin section studies, XRD analysis, and VNIR-SWIR reflectance spectroscopy were utilized to verify the results. The accuracy of SAM classification was numerically calculated using a confusion matrix. The best accuracy of 74.01% and a kappa coefficient of 0.65 were achieved using the SAM method using field samples spectra as the reference. The SAM results were also validated with the mixture tuned matched filtering (MTMF) method. Field investigations showed that more than 90% of the known copper mineralization occurred within the enhanced alteration areas.

Keywords: *Spectral Angle Mapper, ASTER, Hydrothermal Alteration, Porphyry Copper Deposit, Kerman Cenozoic Magmatic Arc.*

1. Introduction

The porphyry copper deposits have received a considerable attention in the remote sensing community in terms of mineral exploration [1-3]. The zones of hypogene hydrothermal alteration and weathering associated with the porphyry copper deposits are large enough to be detected and mapped using multispectral remote sensing data. Most of the known porphyry copper deposits are characterized by a well-developed zonal pattern of mineralization and wall-rock alteration that can be defined by the assemblages of hydrothermal alteration minerals. The mineral assemblages associated with these alteration zones show spectral absorption features in the visible-near infrared (VNIR) and shortwave infrared (SWIR) wavelength regions [4, 5].

The advanced space-borne thermal emission and reflection radiometer (ASTER) covers the VNIR (0.52–0.86 μm), SWIR (1.6–2.43 μm), and thermal infrared (TIR) (8.125–11.65 μm) spectral regions with 14 channels and a high spatial, spectral, and radiometric resolution [6]. The three VNIR bands in ASTER sensors are important sources of information regarding absorption in transition metals, especially Fe and some rare earth elements (REEs). The ASTER SWIR bands are important in distinguishing Al–OH, Fe–OH, Mg–OH, H–O–H, and CO₃ absorption features, thereby providing the potential to map important minerals of hydrothermal alteration such as hydroxyl and carbonate minerals [1, 7].

Mars and Rowan (2006) performed ASTER data by applying multiple band ratios and threshold values for mapping argillic and phyllic zones over the Iranian volcanic sedimentary belt, which includes the present study area [1]. In addition, Tangestani et al. (2008) used ASTER data to analyse a small part of the Iranian volcanic sedimentary belt (the Meiduk and Abdar deposits) with the aim of detecting alteration zones based on directed principal components and spectral angle mapper (SAM) [8]. ASTER/ALI and ASTER/ETM+ images were also employed with the objective of hydrothermal alteration mapping in the NW and SE parts of the Kerman Cenozoic magmatic arc (KCMA) [9, 10]. The KCMA is also known as the Dehaj-Sarduiyeh copper belt. Hosseinjani Zadeh and Honarmand (2017) accomplished discrimination of high- and low-potential mineralization for porphyry copper deposits using ASTER data [11]. Aryanmehr et al. (2018) utilized the Quickbird and Landsat-8 datasets for mapping hydrothermal and gossans alterations in reconnaissance porphyry copper mineralization in the Babbiduyeh area, situated in the Central Iranian Volcano-sedimentary Complex [12]. Furthermore, several studies were carried out to map hydrothermal alteration in local scale using ASTER data on the major porphyry copper deposits in the central part of the KCMA such as Sar Cheshmeh and Darrehzar [13-15].

SAM is a supervised image classification method based on calculation of the angle between the image spectra and reference spectra, treating them as vectors in a feature space with dimensionality equal to the number of bands [16]. The SAM algorithm has previously been applied to hyperspectral and multispectral data for mapping the distribution of hydrothermal alteration [13, 14, 17-19]. In order to achieve more accuracy in hydrothermal alteration mapping, it is necessary to analyse some details before using image processing techniques. Hecker et al. (2008) reported that the SAM classification method may yield different results for the same mineral in the case that different spectra are employed (e.g. image-derived spectra, field-based spectra or a library of standard spectra) [20].

The present study is aimed to verify the effects of different source spectra as the reference on the SAM classification in mapping the distribution of hydrothermal alteration zones. The Kuh-e-Mosahem-Kuh-e-Madvar district, which is a small part in the SE of the central Iranian Cenozoic magmatic belt (CICMB), was selected as the study area. The CICMB is of utmost

importance in terms of porphyry copper mineralization. Due to poor soil development, sparse vegetation cover, abundant outcrop, and arid to semi-arid conditions, this part of the belt is suitable for remote sensing studies.

2. Geological setting and mineralization

The CICMB is the most prominent belt that runs parallel to the Zagros geo-suture for about 1800 km from Azerbaijan in the NW to the north of Makran in the southeast. This belt is a part of the Alpine-Himalayan collisional orogenic belt, which extends from Western Europe to Turkey, across Iran into western Pakistan (Figure 1a) [21]. Magmatism activity in this zone started in the Eocene and reached a climax during the Middle Eocene for volcanic rocks and during the Oligocene-Miocene for plutonic rocks in many parts of Iran [22].

The CICMB is one of the main Cu-bearing regions in the Alpine-Himalayan orogen. Petrogenetic links between porphyry copper mineralization and arc magmatism are well-documented in continental arcs like the Andes, North American Cordillera, Papua New Guinea, and China [26-28].

The study area is located in the KCMA, which is a part of the southeast sector of the CICMB. Figure 1b shows a simplified geological map of the Kuh-e-Mosahem-Kuh-e-Madvar area. The Oligocene-Miocene intrusive rocks were emplaced into the Bahr Aseman (Eocene), Razak (Eocene), and Hezar volcanic complexes. Faulting, fracturing, hydrothermal alteration, and mineralization, both within the intrusive bodies and the associated volcanic rocks, are followed by formation of a supergene environment and an oxidation zone in some of the deposits [29-30].

The Kuh-e-Mosahem-Kuh-e-Madvar area contains several mineral deposits and many important mineral occurrences. Ore deposits of porphyry and vein-type have been identified. The porphyry-type mineralization is dominant, mainly near post-Eocene intrusive bodies in the Eocene volcano-sedimentary complex. The vein type mineralization is controlled by faults showing different trends, and is found both in intrusions and in fine-grained volcanic rocks. The most important porphyry copper deposits in this area are those at Kader, Godekolvary, Iju, Serenu, Chahfiroozeh, Parkam, Meiduk, and Abdar (Figure 1b, Table 1) [24].

Hydrothermal alteration is widespread in this region, producing illite/muscovite (sericite), chlorite, epidote, carbonates, silica, jarosite, and

clay minerals. Field observations and analyses of field samples reveal that sericitization is the most intensive and widespread form of hydrothermal alteration in the study area (Figure 2). Argillization is also common, although not as intensive as the sericitization. Epidotization and carbonitization are associated with chloritization and jarositization occurs in the surface outcrops of hydrothermally altered rocks near the area of

copper mineralization (e.g. at Iju and Parkam). Eight porphyry copper deposits in this area are associated with well-developed zones of hydrothermal alteration including phyllic, argillic, propylitic, silicification, and Jarositization zones (Table 1), with the first three of these zones being the most widely developed. Table 1 presents characteristics of major copper deposits in the study area (modified after [31]).

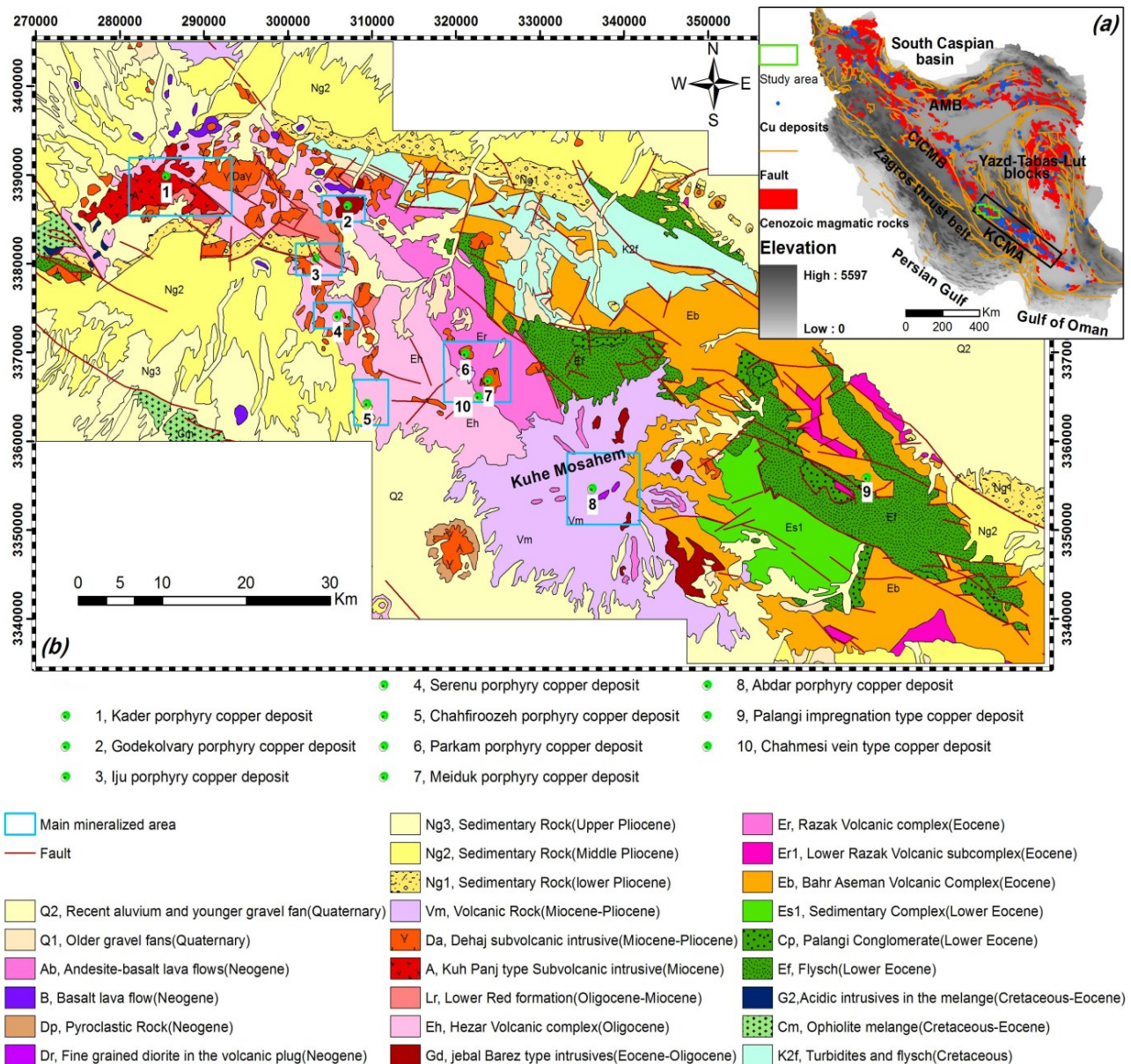


Figure 1. (a) Relief map showing the position of Cenozoic volcanic belts (compiled from [21, 23]). AMB: Alborz magmatic belt, CICMB: Central Iranian Cenozoic magmatic belt, KCMA: Kerman Cenozoic magmatic arc. (b) Simplified geological map of the study area (Adopted from [24, 25]). Locations of the copper deposits are shown (please refer to Table 1).

Table 1. Characteristics of major copper deposits in the study area (modified after [31]).

Deposit	UTM coordinates	Type of mineralization	Host rocks	Main alteration types [†]	Main Altered minerals [†]	Main ore minerals
1. Kader	X: 285503 Y: 3389840	Porphyry	Diorite porphyry, Quartz diorite porphyry	Phyllic, Argillic, Propylitic, Silicification	Muscovite, Kaolinite, Illite, Quartz, Natroalunite	Pyrite, Chalcopyrite, Chalcocite, Covellite
2. Godekolvary	X: 307128 Y: 3386478	Porphyry	Diorite porphyry, Granodiorite, Andesite	Argillic, Phyllic, Propylitic, Silicification	Kaolinite, Muscovite, Montmorillonite, Quartz, Chlorite, Epidote	Pyrite, Chalcopyrite
3. Iju	X: 303315 Y: 3380542	Porphyry	Diorite porphyry, Quartz diorite porphyry	Phyllic, Argillic, Potassic, Propylitic, Jarositization	Muscovite, Illie, Quartz, Kaolinite, Albite, Chlorite	Pyrite, Chalcopyrite, Chalcocite
4. Serenu	X: 305954 Y: 3374148	Porphyry	Diorite porphyry, Quartz diorite porphyry, Andesite	Phyllic, Argillic, Propylitic, Potassic	Muscovite, Illie, Quartz, Albite, Orthoclase, Kaolinite, chlorite Montmorillonite	Pyrite, Chalcopyrite
5. Chahfiroozeh	X: 309441 Y: 3364244	Porphyry	Granodiorite porphyry	Phyllic, Potassic, Propylitic	Muscovite, Illie, Quartz, Albite, Orthoclase	Malachite, Azurite, Chrysocolla, Pyrite, Chalcopyrite
6. Parkam	X: 321121 Y: 3369859	Porphyry	Diorite porphyry, Micro diorite porphyry	Phyllic, Argillic, Potassic, Propylitic, Jarositization, Silicification	Muscovite, Illie, Quartz, Jarosite, Albite, Orthoclase, Kaolinite	Pyrite, Chalcopyrite, Malachite
7. Meiduk	X: 323885 Y: 3366900	Porphyry	Diorite porphyry	Phyllic, Argillic, Potassic, Propylitic	Muscovite, Illie, Quartz, Jarosite, Albite, Orthoclase, Kaolinite, Montmorillonite	Pyrite, Chalcopyrite, Chalcocite, Malachite
8. Abdar	X: 336271 Y: 3354694	Vein and Porphyry	Granodiorite porphyry, Dasiteporphyry, Andesite and diorite	Phyllic, Argillic, Propylitic	Muscovite, Illie, Quartz, Albite, Kaolinite, Montmorillonite, Chlorite	Pyrite, Chalcopyrite, Galena, Malachite
9. Palangi	X: 368910 Y: 3355907	Impregnation	Andesite and pyroclastites	Carbonatization, Propylitic, Chloritization, Sericitization, Silicification	Chlorite, Epidote, Calcite, Quartz	Chalcopyrite, Malachite, Azurite, Chalcocite, Bornite
10. Chahmesi	X: 322676 Y: 3365076	Vein	Andesite, Diorite porphyry	Propylitic, Silicification	Chlorite, Epidote, Quartz	Chalcopyrite, Chalcocite, Sphalerite, Malachite, Azurite, Galena

[†]Based on field observations, thin section studies, spectral measurements, and XRD analysis (This study).



Figure 2. Field photographs of typical alteration zones in the study area. (a) Phyllic alteration zone with silica veinlets, (b) iron oxides (hematite and goethite) with argillic alteration, (c) phyllic alteration and jarositization, (d) phyllic alteration stained with iron oxide and hydroxide minerals, (e) phyllic alteration, (f) regional view of the central alteration zone, (g) phyllic and propylitic alteration zones, and (h) regional view of propylitic alteration.

3. Spectral characteristics of hydrothermal alteration and ASTER data

Hydrothermal alteration related to porphyry Cu deposits usually exhibits a concentric zonal pattern zoned from potassic zone at the core outward through phyllic (quartz–sericite–pyrite), argillic (quartz–kaolinite–montmorillonite), and propylitic zones (epidote–calcite–chlorite) [31-32]. The spectral reflectance characteristics of minerals in the phyllic, argillic, and propylitic hydrothermal alteration zones provide a basis for identifying hydrothermally altered rocks

associated with porphyry copper deposits in semi-arid and arid regions. The hydrothermal alteration zones are characterised by mineral assemblages containing at least one mineral that exhibits diagnostic spectral absorption features.

As most hydrothermal alteration minerals have absorption features in the SWIR region of the electromagnetic spectrum, multispectral SWIR data are commonly used for hydrothermal alteration mapping. ASTER SWIR bands are positioned to define absorption features of common minerals that are typically formed by

hydrothermal alteration processes. Thus, SWIR images of ASTER sensor have successfully been used for mapping some hydrothermal alteration minerals such as illite/muscovite (sericite), kaolinite, epidote, calcite, and chlorite [1]. For the present study area, the VNIR and SWIR spectral regions of ASTER are expected to enable discrimination of the main alteration minerals.

Hydrothermal alteration, which develops within both intrusive and volcanic rocks, is widespread over the present study area, and has the potential to host porphyry copper mineralization. Important absorption features of the minerals associated with hydrothermal alteration zones within the SWIR bands of the ASTER sensor is summarized in Table 2 [33].

Table 2. Some important absorption features of the minerals associated with hydrothermal alteration zones in the SWIR bands of ASTER sensor [1, 33-36].

ASTER band	Spectral range (µm)	Absorption		Index minerals	Alteration type
		Source(s)	Wavelength (µm)		
5	2.145–2.185	Al-OH	2.170	Kaolinite	Argillic
				Kaolinite	Argillic
6	2.185–2.225	Al-OH	2.200	Montmorillonite	Argillic
				Muscovite (sericite) and illite	Phyllic
				Muscovite (sericite) and illite	Phyllic
8	2.295–2.365	Al-OH	2.380	Muscovite (sericite) and illite	Phyllic
		Fe, Mg-OH, and CO ₃	2.330	Epidote, chlorite, and carbonate	Propylitic

4. Material and methods

In order to achieve the aim of this research, it was necessary to collect different reference spectra in the first step. Three types of reference spectra including image spectra, the spectra of field samples (as obtained using a FieldSpec3® spectroradiometer), and spectra from a standard library (USGS) were gathered. ASTER VNIR/SWIR images were classified and compared using the SAM method by applying various types of reference spectra. Accuracy assessment of the results was performed through fieldworks and laboratory studies. The MTF method was also applied using endmembers produced by pixel purity index (PPI) method to compare hydrothermal alteration map with those obtained by SAM classification.

4.1. Pre-processing of ASTER data

Level-1B (radiance at sensor) and cloud-free ASTER images, acquired on 25 July 2001, were selected for this study. Crosstalk correction was applied using the crosstalk correction software (CCS) provided by the Earth Remote Sensing Data Centre (ERSDAC) [37]. This correction was performed to reduce the SWIR crosstalk effect, which is caused by the dispersion of incident light of the band 4 detector to other detectors in the SWIR region.

ASTER level-1B radiance data were converted to surface reflectance using fast line-of-sight atmospheric analysis of spectral hypercubes (FLAASH) software [38]. The images were pre-georeferenced to a UTM Zone 40 north projection with WGS-84 datum and once more orthorectified and reprojected using a digital

elevation model and orthorectified Landsat ETM+ imagery. The six scenes were clipped and combined to form a single image mosaic with an approximate area of 5787 km².

4.2. Reference spectra collection

4.2.1. Library spectra

The United States Geological Survey (USGS) spectral library (2007) was used to choose the VNIR/SWIR reflectance spectra of important hydrothermal alteration minerals and the secondary iron oxide/hydroxide bearing minerals of relevance to the present study [39]. The selected spectra were re-sampled to match either the response of ASTER instrument. Figure 3 represents the library spectra that were prepared to use in the SAM algorithm.

4.2.2. Rock samples spectra

Figure 4 shows the field spectra of samples obtained from various alteration zones, as measured by a FieldSpec3® spectroradiometer (Analytical Spectral Devices, Inc., Boulder, CO, USA). The spectra of the samples from the phyllic zone show a strong absorption feature at 2.2 µm and a low absorption at 2.4 µm due to sericite (Figures 3a and 4a). Kaolinite in the argillic zone shows absorption features at 2.18 and 2.4 µm (Figures 3a and 4b). The jarosite, goethite, and hematite minerals associated with the phyllic zone show a strong reflectance at 0.74 µm and absorption at 0.4 µm (Figures 3b and 4a). The propylitic zone, which is characterised by chlorite and epidote, has a strong absorption at 2.35 µm (Figures 3a and 4b).

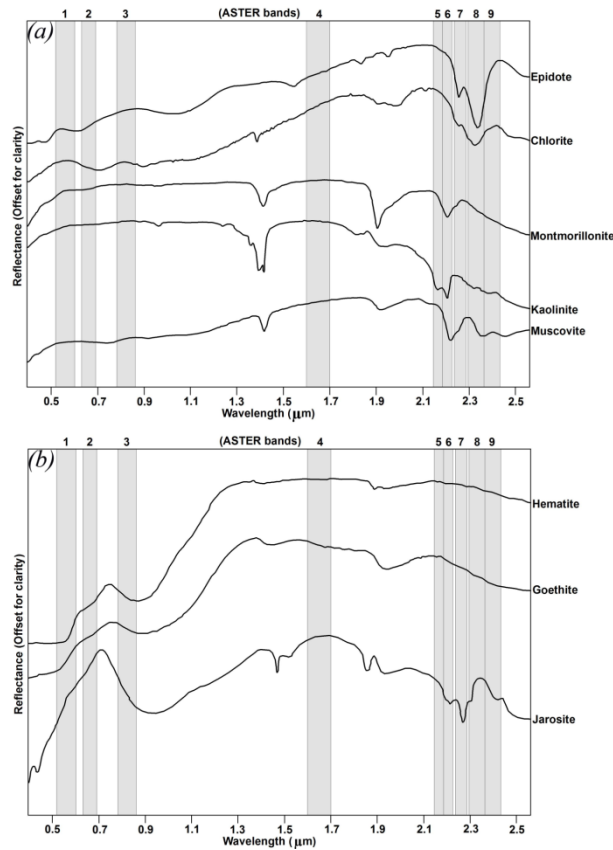


Figure 3. (a) Laboratory reflectance spectra of important hydrothermal alteration minerals and (b) iron oxide/hydroxide bearing minerals. ASTER bands' widths are shown in the figure (after [30]).

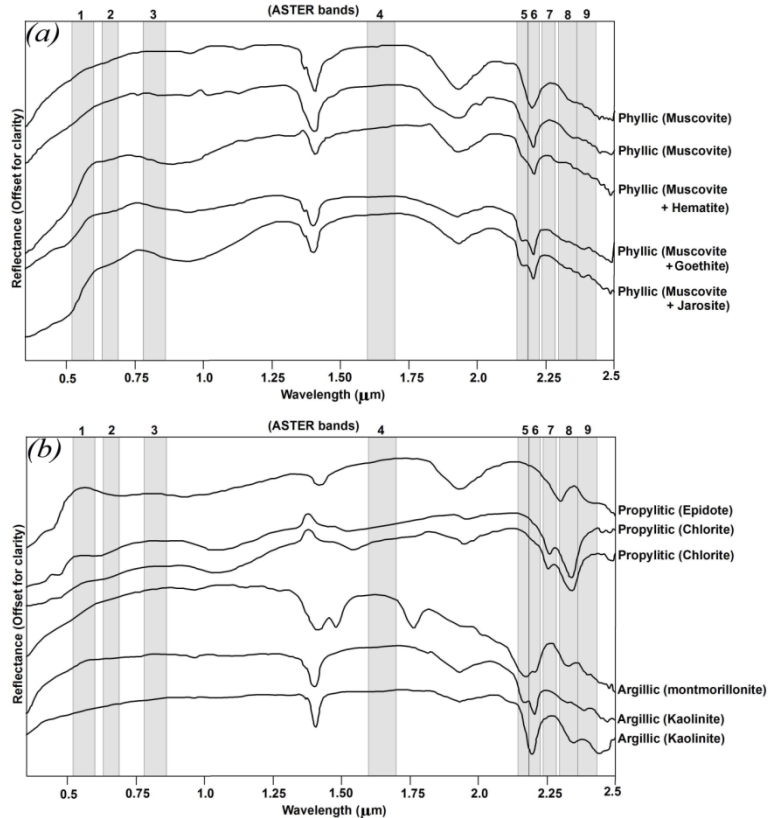


Figure 4. Spectra of the samples from the (a) phyllic, (b) argillic, and propylitic zones measured by a spectroradiometer.

4.2.3. Image spectra

Image spectra can be directly extracted through Z-profiling of known hydrothermal alteration zones. This type of image spectra was also used in the SAM algorithm. The application of MTMF method requires pure image spectra (endmembers). Endmembers can be derived by applying minimum noise fraction (MNF), pixel purity index (PPI), and n-dimensional visualization techniques from ASTER images. A challenging task is to identify endmember pixels whose spectra are extreme, especially in high-dimensional image data. This difficulty arises because most pixels contain varying proportions of different materials [16, 40, 41]. A

spectral mixture model is a physically-based model in which a mixed spectrum is modelled as a combination of pure spectra that are referred to as endmembers.

Figure 5 shows the image-derived spectra of the major hydrothermal alteration types for VNIR/SWIR bands of ASTER data in the study area. In order to enable the identification of minerals, these spectra were compared with known spectra from the USGS spectral library and with data from samples collected in the field as part of ground truthing (i.e. XRD analysis, observation of thin sections, and spectral measurements).

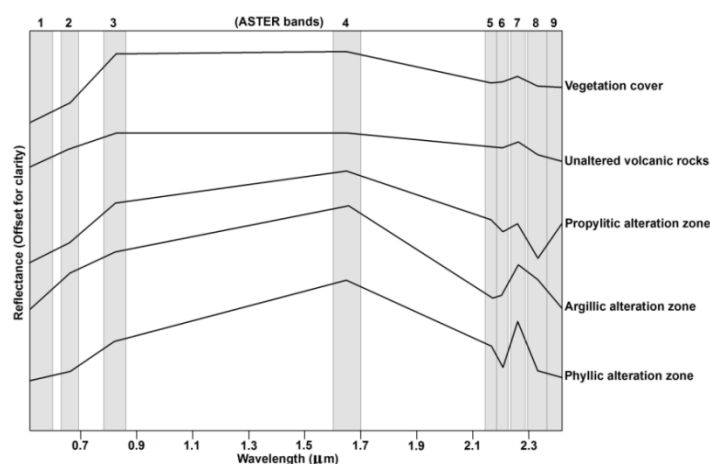


Figure 5. Image spectra of selected endmembers used as reference spectra in MTMF method.

4.3. Image classification

4.3.1. SAM

SAM is known as a powerful and rapid classification method that operates based on the degree of similarity between image spectra and reference spectra. The reference spectra can be chosen from either laboratory or field spectra or extracted from the image. SAM compares the angle between the reference spectrum and each pixel vector in n-dimensional space, with smaller angles indicating a closer match to the reference [16]. SAM depends on an overall spectral fit rather than the shape of individual absorption features. The spectral angle is the average fit over the entire spectral range of the dataset used in the classification. This may include non-diagnostic parts of the spectrum as well as spectral trends that influence the absorption depth and the positions of superimposed features [20].

4.3.2. MTMF

MTMF is a hybrid method based on a combination of well-known signal-processing methodologies and linear mixture theory. This

method benefits the ability to map a single known target, without the knowledge of all endmember signatures, with the leverage of mixed pixel models, including placing constraints on feasibility. MTMF suppresses background noise and estimates the sub-pixel abundance of a single target material. The MTMF method includes three main steps: (1) a MNF transformation of apparent reflection data [42], (2) matched filtering for abundance estimation, and (3) mixture tuning to identify infeasible or false-positive pixels [43].

4.4. Accuracy assessment

The collection of field data is an important part of any remote sensing study. With the aim of assessing the accuracy of the image processing results, 15 field sites were selected for ground control and sampling, from where 227 samples were collected according to a research project agreement (No. 4028) with the Institute of Science and High Technology and Environmental Sciences, Graduate University of Advanced Technology, Kerman, Iran. This follow-up work included visits to all the known sites of copper

mineralization reported in previous studies as well as the alteration zones identified in the present study (Table 1), in an attempt to better understand the nature of hydrothermal alteration in each site. At each station, altered rock samples were collected along with GPS reading and taking photographs of altered outcrops (as seen in Figure 2). After that, rock samples were prepared for thin section studies and XRD analysis. The spectra of the representative samples from altered zones were also measured using a FieldSpec3® spectroradiometer. Finally, the accuracy of the classified images was examined using a confusion matrix [44].

5. Results

Figure 6 shows the eigenvalues of the nine output MNF images of the ASTER VNIR/SWIR bands. As the hydrothermal alterations are seen in the MNF components 2, 3, and 4, a three-band false-colour composite image (RGB: MNF2,

MNF3, MNF4) was selected to delineate hydrothermal alteration zones (Figure 7). This image shows a good result in terms of enhancing the altered areas, which are shown by white to cyan pixels.

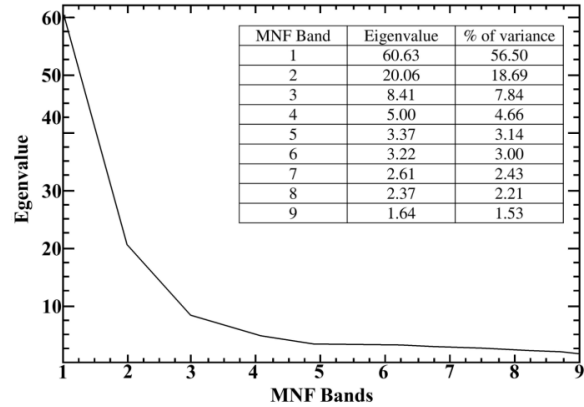


Figure 6. The MNF eigenvalues plot of the nine eigen-images of the ASTER data.

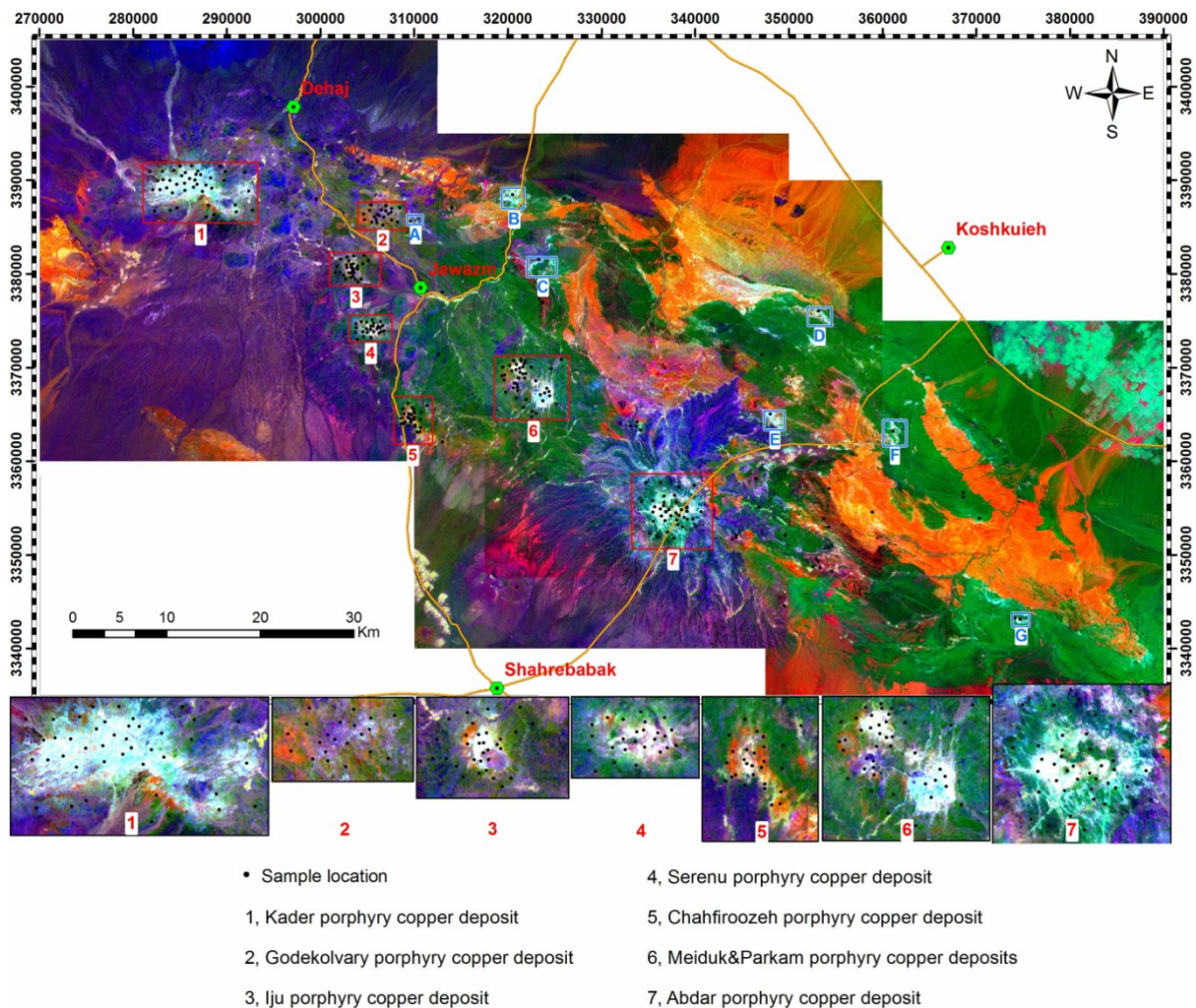


Figure 7. A colour composite of MNF bands (MNF2=red, MNF3=green, MNF4= blue). The larger images of the mineralized areas are shown. The altered areas are displaying in white to cyan colours. The areas A to G show weak alterations that are not associated with mineralization.

The PPI was applied over the first six MNF images that were extracted from ASTER VNIR/SWIR bands with higher eigenvalues containing 93.83% of the total data variance (see Figure 6). Five main endmembers were identified using the PPI technique from the six MNF images: muscovite/illite, kaolinite/montmorillonite, chlorite/epidote, unaltered units in volcanic rocks, and green vegetation (Figure 7). The muscovite/illite endmember is generally restricted to the phyllic alteration zone. The kaolinite/montmorillonite endmember is limited to the argillic alteration zone, and the chlorite/epidote endmember corresponds to the propylitic alteration zone, although there is some overlap in the occurrence

of the associated minerals. In this research, we sought to map the distribution of three alteration zones over the eight copper–mineralization districts using the endmembers derived from the n–dimensional endmember visualization method as the reference spectra for MTMF classification. Figure 8 shows the final image-derived from MTMF analysis.

The SAM classification was applied on the ASTER VNIR/SWIR data using the USGS spectral library (SAM1), spectra from field samples (SAM2), and image spectra derived from ASTER data (SAM3). Figures 9 to 11 show the results obtained using the SAM1, SAM2, and SAM3 classifications for different spectral types.

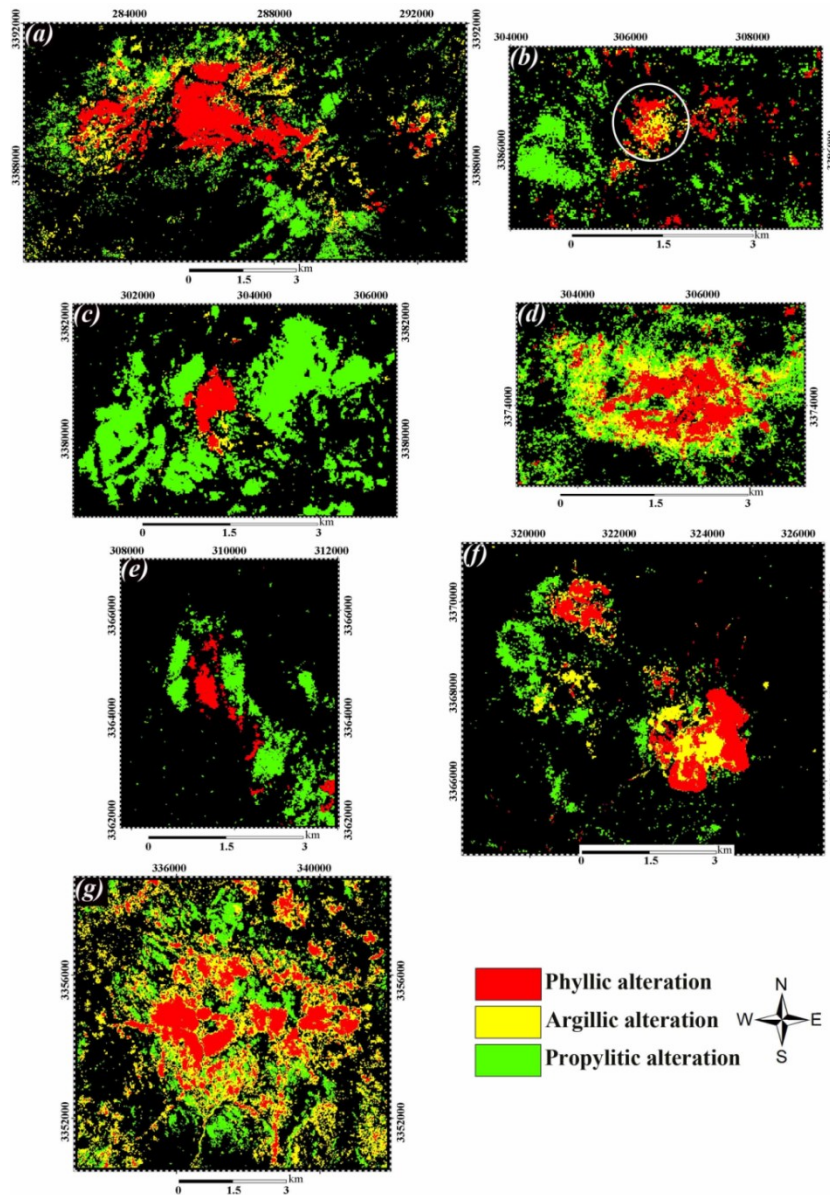


Figure 8. MTMF results for hydrothermal alteration mapping using the endmember spectra in Figure 7, around the porphyry type deposits in the study area. (a) Kader, (b) Godekolvary, (c) Iju, (d) Serenu, (e) Chahfiroozeh, (f) Meiduk and Parkam, (g) Abdar.

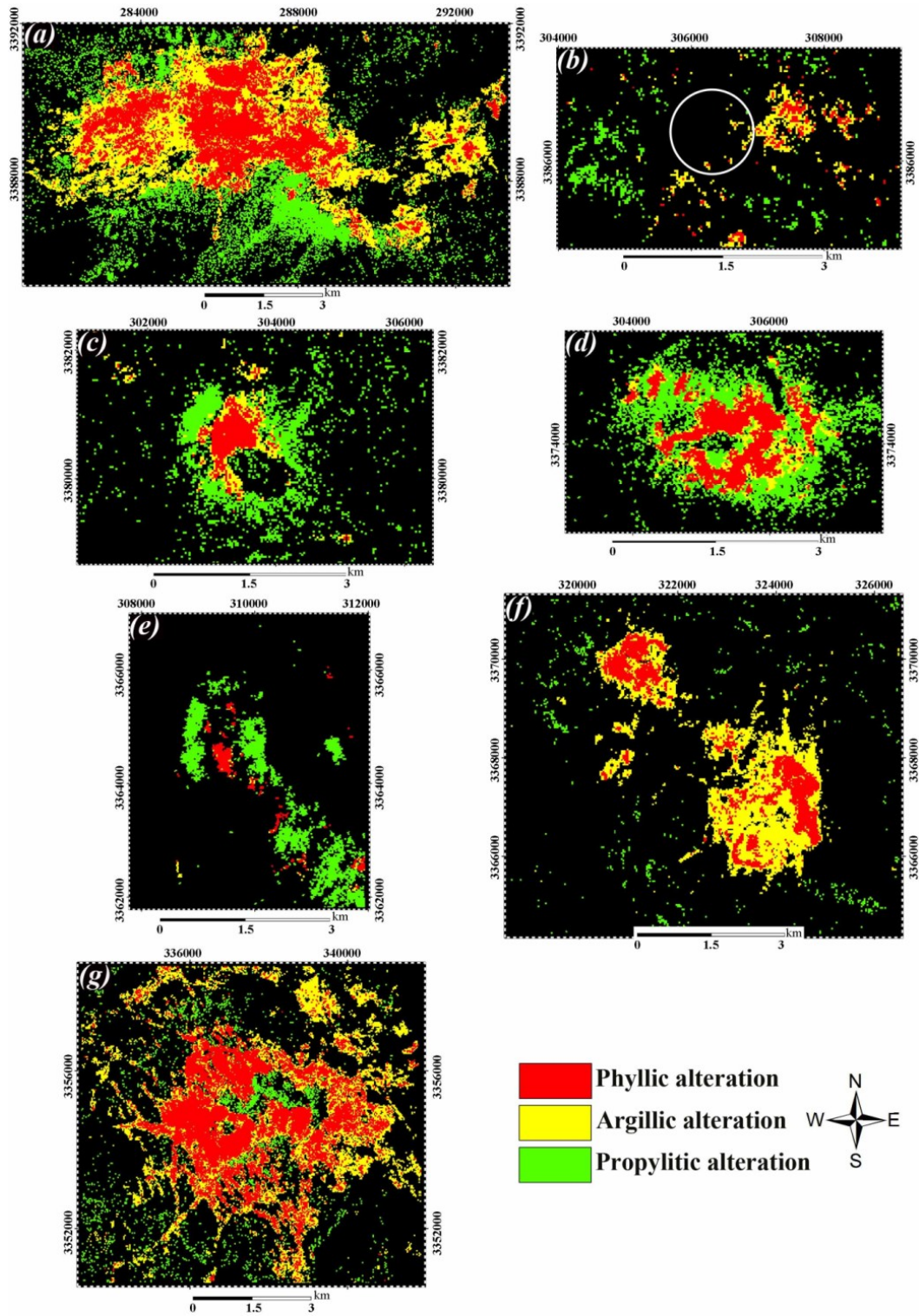


Figure 9. Results of SAM classification using USGS spectral library (SAM1). (a) Kader, (b) Godekolvary, (c) Iju, (d) Serenu, (e) Chahfiroozeh, (f) Meiduk and Parkam, (g) Abdar.

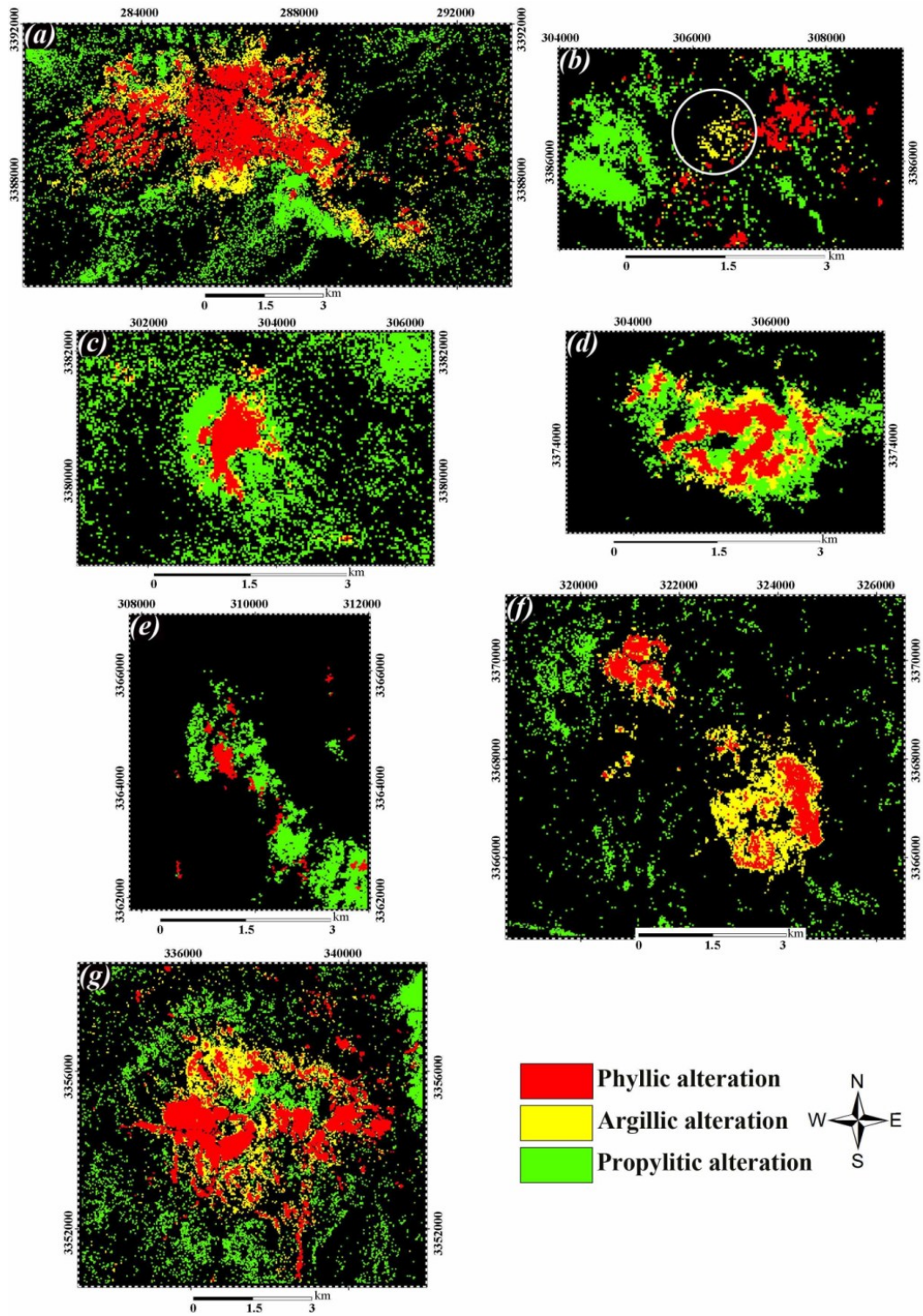


Figure 10. Results of SAM classification using spectra from the field samples (SAM2). (a) Kader, (b) Godekolvary, (c) Iju, (d) Serenu, (e) Chahfiroozeh, (f) Meiduk and Parkam, (g) Abdar.

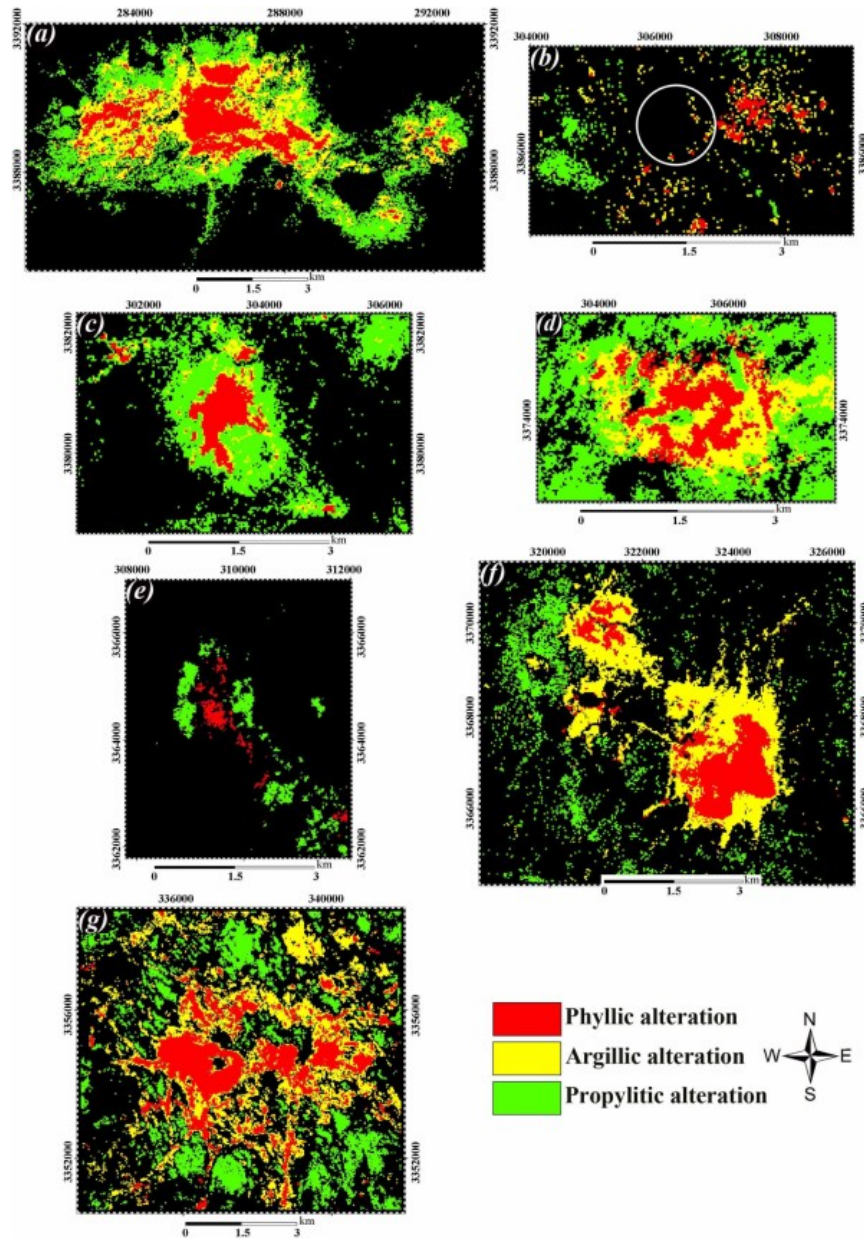


Figure 11. Results of SAM classification using image-derived spectra (SAM3). (a) Kader, (b) Godekolvary, (c) Iju, (d) Serenu, (e) Chahfiroozeh, (f) Meiduk and Parkam, (g) Abdar.

After applying these techniques, the results were compared using the selected sites as ground control points, from where samples were collected for XRD analysis, spectral measurement of representative samples using a FieldSpec3® spectroradiometer, and for observation in thin sections (see Table 1).

Table 3 shows the accuracy assessment matrix of the SAM and MTF analysis results based on 227 samples. Although, visual comparison of the SAM and MTF images for hydrothermal alteration mapping (Figures 8 to 11), in general, show similar results, detailed direct comparison of the mapping results using a confusion matrix approach demonstrates that their similarities are not as great as may be thought from visual

comparison. As stated above, the SAM classification was performed using three different spectra. The highest accuracy was obtained using the SAM2 approach with field samples spectra (74.01%; kappa coefficient, 0.65). Similar accuracies were obtained for SAM3 and SAM1 classifications using the image-derived spectra and the USGS spectral library, respectively. The overall accuracy estimated for zones of phyllic and propylitic alteration is higher than that for argillic zones. The MTF-based classification yielded a better result than SAM, especially for the phyllic zone. The overall estimated accuracy for the MTF analysis was 81.5% (kappa coefficient, 0.71).

Table 3. Accuracy assessment matrices for different classification methods.

	Phyllic	Argillic	Propylitic	Unaltered	Total	Percent
a) Classification accuracy assessment for the spectral angle mapper approach using USGS spectral library (SAM1).						
Phyllic	87	4	8	2	101	86.14
Argillic	14	22	8	2	46	47.83
Propylitic	4	0	39	2	45	86.67
Unaltered	9	8	8	10	35	28.57
Total	114	34	63	16	227	
Percent	76.32	64.71	61.90	62.50		69.60
Kappa coefficient: 0.59						
b) Classification accuracy assessment for the spectral angle mapper approach using spectra from field samples (SAM2).						
Phyllic	89	2	5	2	98	90.82
Argillic	13	24	6	2	45	53.33
Propylitic	5	2	44	1	52	84.61
Unaltered	7	6	8	11	32	34.37
Total	114	34	63	16	227	
Percent	78.07	70.59	69.84	68.75		74.01
Kappa coefficient: 0.65						
c) Classification accuracy assessment for the spectral angle mapper approach using image spectra (SAM3).						
Phyllic	88	6	9	1	104	84.61
Argillic	16	24	7	3	50	48.00
Propylitic	5	0	39	2	46	84.78
Unaltered	5	4	8	10	27	37.04
Total	114	34	63	16	227	
Percent	77.19	70.59	61.90	62.50		70.92
Kappa coefficient: 0.61						
d) Classification accuracy assessment for the Mixture Tuned Matched Filtering (MTMF) approach.						
Phyllic	95	2	2	1	101	94.06
Argillic	8	27	3	1	39	69.23
Propylitic	5	0	50	1	55	90.91
Unaltered	6	5	8	13	32	40.62
Total	114	34	63	16	227	
Percent	83.33	79.41	79.36	81.25		81.50
Kappa coefficient: 0.71						

6. Discussion

Figure 5 shows the image-derived spectra of the phyllic, argillic, and propylitic alteration zones for VNIR/SWIR data. Comparison of the laboratory reflectance spectra for selected samples (as measured by spectroradiometer, Figure 4) and the corresponding spectra derived from the images (Figure 5) reveals that the overall shapes of the ASTER image spectra are slightly different from the United States Geological Survey (USGS) laboratory spectra (Figure 3) due to the effects of several factors that influence the image spectra (these effects are absent in the laboratory conditions). These effects include the presence of variable mixtures of minerals, the products of surface weathering, vegetation, grain size variations, and residual atmospheric absorption features.

The SAM-classified images using the USGS spectral library (SAM1), spectra measured from field samples (SAM2), and image spectra (SAM3) give approximately similar results but the accuracy assessment method using confusion

matrix showed that SAM2 was more accurate (see Table 3). The MTMF image is generally in good agreement with the mapped distribution of hydrothermally altered rocks in the study area. A comparison between the MTMF mapping result (Figure 8) and the SAM2 (using field samples spectra) classification result (Figure 10) reveals similar patterns of alteration zones, although with marked differences in some areas. The MTMF classification method is superior to the SAM2 classification method in its ability to enhance various alteration zones, especially in the Kader, Godekolvary, Serenu, and Abdar areas (compare Figures 8 and 10). There exists one alteration zone in the Godekolvary area, which is enhanced in the MTMF classification image, as outlined in Figure 8b by white circle, but is not prominent in the SAM1–3 classification image (see Figures 9b, 10b, and 11b). The argillic zone in the Kader area is more strongly enhanced in the MTMF classification image than in the SAM (1–3) images. The areal extent of the enhanced argillic zone in the SAM2 image is inaccurate (compare

Figures 8a and 10a). Compared with the SAM images, the propylitic zone is more strongly enhanced in all areas in the MTMF image (see Table 3).

The Meiduk open-pit mine (see Figure 2) is the only site in the study area that has been excavated; the fresh and altered material is exposed in and around the pit. This material that is rich in sericite and clay minerals was mapped more accurately using MTMF and SAM2 methods.

SAM depends on an overall spectral fit rather than the shape of individual, diagnostic absorption features [42]. In contrast, MTMF is a mixed pixel classification, in which a partial unmixing method suppresses the background noise and estimates the sub-pixel abundance of a single target material [20]. This may explain why the MTMF technique yielded a better result than did the SAM method. The results obtained for various sites of mineralization indicate that the MTMF mapping method can be used to produce a reliable map of alteration at the preliminary stage of mineral exploration, and this algorithm can be used for further exploratory investigations.

Field and laboratory studies confirmed that the altered areas enhanced using image processing techniques are clearly visible at the surface (Figure 2). The sites classified as altered areas in the processed images consist of rocks that contain sericite, illite, kaolinite, montmorillonite, chlorite, epidote, quartz, smectite, albite, calcite, alunite, pyrophyllite, goethite, jarosite, and orthoclase, with the most common of these minerals being sericite, illite, kaolinite, and chlorite. These areas also show the development of secondary iron minerals at the surface, particularly in phyllic alteration zone. Table 1 lists the results of XRD analyses of the major phases of alteration minerals in the study area. In addition to these areas of alteration, several new anomalous areas (areas A–G, see Figure 7) were also sampled, revealing the areas of alteration affected by kaolinitization, sericitization, and silicification. Field observations indicated that these areas were weakly altered compared with the mineralized areas, and no copper mineralization was observed. More than 90% of the existing copper mineralization was located within the interpreted areas of alteration. The remaining 10% of the copper mineralization was of vein type that did not show prominent alteration haloes at the surface.

7. Conclusions

The accuracy of image processing for spectrum-based methods such as SAM depends on

the input spectra. This study concentrated on studying the effect of input spectra on the SAM results for hydrothermal alteration mapping. The results of accuracy assessment showed little difference in the application of image spectra, spectra from field samples, and spectra from the USGS spectral library for hydrothermal alteration mapping by the SAM method, although the highest accuracy was obtained using the field samples spectra. The spectra derived from the PPI method, used as the reference spectra in the MTMF method, led to perform a more accurate classification than the results obtained from the SAM method. Field studies confirmed that the MTMF method was reliable in terms of mapping hydrothermal alteration haloes during the preliminary stages of exploration for porphyry-type mineralization. The results of field and laboratory studies revealed that more than 90% of the mineralized areas occurred within the interpreted alteration zones; the remaining mineralized areas were of vein-type mineralization.

Acknowledgments

We gratefully acknowledge the research fund provided for this project (No. 4028) by the Institute of Science and High Technology and Environmental Sciences, Graduate University of Advanced Technology, Kerman, Iran. We also wish to thank the Kerman Office of Mines and Industries, and the national Iranian copper industries company for assisting with logistics during fieldwork and when collecting samples.

References

- [1]. Mars, J.C. and Rowan, L.C. (2006). Regional mapping of phyllic and argillic altered rocks in the Zagros magmatic arc, Iran, using Advanced Spaceborne Thermal Emission and Reflection Radiometer (ASTER) data and logical operator algorithms. *Geosphere*. 2 (3): 161-186.
- [2]. Barak, S., Bahroudi, A. and Jozanikohan, G. (2018). Exploration of Kahang porphyry copper deposit using advanced integration of geological, remote sensing, geochemical, and magnetism data. *Journal of Mining Environment*. 9 (1): 19-39.
- [3]. Ayoobi, I. and Tangestani, M.H. (2018). Evaluation of subpixel unmixing algorithms in mapping the porphyry copper alterations using EO-1 Hyperion data, a case study from SE Iran. *Remote Sensing Applications: Society and Environment*. 10: 120-127.
- [4]. Abrams, J., Brown, D., Lepley, L. and Sadowaski, R. (1983). Remote sensing for porphyry copper

deposits in Southern Arizona. *Econ. Geol.* 78 (4): 591-604.

[5]. Neal, L.C., Wilkinson, J.J., Mason, P.J. and Chang, Z. (2018). Spectral characteristics of propylitic alteration minerals as a vectoring tool for porphyry copper deposits. *J. Geochem. Explor.* 184: 179-198.

[6]. Yamaguchi, Y., Wyman, D.A., Xu, J.F., Zhao, Z.H., Jian, P. and Zi, F. (1998). Overview of Advanced Spaceborne Thermal Emission and Reflection Radiometer (ASTER). *IEEE T. Geosci. Remote.* 36 (4): 1026-1071.

[7]. Rowan, L.C., Hook, S.J., Abrams, M.J. and Mars, J.C. (2003). Mapping hydrothermally altered rocks at Cuprite, Nevada, using the advanced space borne thermal emission and reflection radiometer (ASTER), a new satellite-imaging system. *Econ. Geol.* 98 (5): 1018-1027.

[8]. Tangestani, M.H., Mazhari, N., Agar, B. and Moore, F. (2008). Evaluating Advanced Spaceborne Thermal Emission and Reflection Radiometer (ASTER) data for alteration zone enhancement in a semi-arid area, northern Shahr-e-Babak, SE Iran. *Int. J. Remote Sens.* 29 (10): 2833-2850.

[9]. Honarmand, M., Ranjbar, H. and Shahabpour, J. (2011). Application of Spectral Analysis in Mapping Hydrothermal Alteration of the Northwestern Part of the Kerman Cenozoic Magmatic Arc, Iran. *Journal of Sciences, Islamic Republic of Iran.* 22 (3): 221-238.

[10]. Honarmand, M., Ranjbar, H. and Shahabpour, J. (2012). Application of principal component analysis and spectral angle mapper in the mapping of hydrothermal alteration in the Jebal-Barez Area, Southeastern Iran. *Resour. Geol.* 62 (2): 119-139.

[11]. Hosseinjani Zadeh, M. and Honarmand, M. (2017). A remote sensing-based discrimination of high- and low-potential mineralization for porphyry copper deposits; a case study from Dehaj-Sarduiyeh copper belt, SE Iran. *Eur. J. Remote Sens.* 50 (1): 332-342.

[12]. Aryanmehr, H., Hosseinjanizadeh, M., Honarmand, M. and Naser, F. (2018). Hydrothermal alterations mapping using Quickbird and Landsat-8 data, a case study from Babbiduyeh, Kerman province, Iran. *Journal of Mining and Environment.* 9 (1): 41-52.

[13]. Salimi, A., Ziaii, M., Amiri, A. and Hosseinjani Zadeh, M. (2017). Sub-pixel classification of hydrothermal alteration zones using a kernel-based method and hyperspectral data; A case study of Sarcheshmeh Porphyry Copper Mine and surrounding area, Kerman, Iran. *Journal of Mining and Environment.* 8 (4): 555-565.

[14]. Shahriari, H., Ranjbar, H., Honarmand, M. and Carranza, E.J.M. (2014). Selection of Less Biased Threshold Angles for SAM Classification Using the Real Value-Area Fractal Technique, *Resour. Geol.* 64: 301-315.

[15]. Shahriari, H., Ranjbar, H. and Honarmand, M. (2013). Image segmentation for hydrothermal alteration mapping using PCA and concentration-area fractal model. *Nat. Resour. Res.* 22 (3): 191-206.

[16]. Kruse, F.A., Lefkoff, A.B., Boardman, J.W., Heidebrecht, K.B., Shapiro, A.T., Barloon, P.J. and Goetz, A.F.H. (1993). The Spectral Image Processing System (SIPS)—interactive visualization and analysis of imaging spectrometer data. *Remote Sens. Environ.* 44 (2-3): 145-163.

[17]. Honarmand, M., Ranjbar, H. and Shahabpour, J. (2013). Combined use of ASTER and ALI data for hydrothermal alteration mapping in the northwestern part of the Kerman Magmatic Arc, Iran. *Int. J. Remote Sens.* 34 (6): 2023-2046.

[18]. Dai, J., Qu, X. and Song, Y. (2018). Porphyry Copper Deposit Prognosis in the Middle Region of the Bangonghu–Nujiang Metallogenic Belt, Tibet, Using ASTER Remote Sensing Data. *Resour. Geol.* 68 (1): 65-82.

[19]. Yousefi, S.J., Ranjbar, H., Alirezaei, S., Dargahi, S. and Lentz, D.R. (2018). Comparison of hydrothermal alteration patterns associated with porphyry Cu deposits hosted by granitoids and intermediate-mafic volcanic rocks, Kerman Magmatic Arc, Iran: Application of geological, mineralogical and remote sensing data. *J. Afr. Earth Sci.* 142: 112-123.

[20]. Hecker, C., Van der Meijde, M., van der Werff, H. and van der Meer, F.D. (2008). Assessing the Influence of Reference Spectra on Synthetic SAM Classification Results. *IEEE T. Geosci. Remote.* 46 (12): 4162-4172.

[21]. Shafiei, B., Haschke, M. and Shahabpour, J. (2009). Recycling of orogenic arc crust triggers porphyry Cu mineralization in Kerman Cenozoic arc rocks, southeastern Iran. *Miner. Deposita.* 44 (3): 265-283.

[22]. Alavi, M. (1980). Tectono-stratigraphic evolution of the Zagros side of Iran. *Geology.* 8: 144-149.

[23]. Bazin, D. and Hubner, H. (1969). Copper deposits in Iran. Report No.13, Tehran, Iran: Ministry of Economy Geological Survey of Iran.

[24]. Dimitrijevic, M.D. (1973). Geology of the Kerman region. Report No. 52, Tehran, Iran: Ministry of Economy Geological Survey of Iran.

[25]. Saric, V. and Mijalkovic, N. (1973). Metallogenic map of Kerman region, 1:500000 scale. In: Exploration for ore deposits in Kerman region. Report No. 53, Tehran, Iran: Ministry of Economy Geological Survey of Iran.

[26]. Sillitoe, R.H. (1972). A plate tectonic model for the origin of porphyry copper deposits. *Econ. Geol.* 67 (2): 184-197.

- [27]. Hassanzadeh, J. (1993). Metallogenic and tectono–magmatic events in the SE sector of the Cenozoic active continental margin of Iran (Shahr–e–Babak area, Kerman province). Unpublished Ph.D thesis, University of California, USA.
- [28]. Wang, Q., Wyman, D.A., Xu, J.F., Zhao, Z.H., Jian, P. and Zi, F. (2007). Partial melting of thickened or delaminated lower crust in the middle of Eastern China: implications for Cu–Au mineralization. *J. Geol.* 115 (2): 149–161.
- [29]. Shahabpour, J. (1982). Aspects of alteration and mineralization at the SarCheshmeh copper–molybdenum deposit, Kerman, Iran. PhD thesis (unpublished), University of Leeds.
- [30]. Livo, K.E., Clark, R.N. and Knepper, D.H. (1993). Spectral plot program for accessing the USGS digital spectral library database with MS–DOS personal computers. USGS Open–file, Denver, Colorado, Report No. 93–593.
- [31]. Geological Survey of Iran (GSI). (1973). Exploration for ore deposits in Kerman region. Report No. Yu/53, Tehran, Iran. Ministry of Economy Geological Survey of Iran.
- [32]. Lowell, J.D. and Guilbert, J.M. (1970). Lateral and vertical alteration–mineralization zoning in porphyry ore deposits. *Econ. Geol.* 65 (4): 373–408.
- [33]. Shahriari, H., Honarmand, M. and Ranjbar, H. (2015). Comparison of multi-temporal ASTER images for hydrothermal alteration mapping using a fractal-aided SAM method. *Int. J. Remote Sens.* 36 (5): 1271–1289.
- [34]. Hunt, G.R. (1977). Spectral signatures of particulate minerals in the visible and near infrared. *Geophysics.* 42 (3): 501–513.
- [35]. Hunt, G.R. and Ashley, R.P. (1979). Spectra of altered rocks in the visible and near infrared. *Econ. Geol.* 74 (7): 1613–1629.
- [36]. Rowan, L.C., Schmidt, R.G. and Mars, J.C. (2006). Distribution of hydrothermally altered rocks in the RekoDiq, Pakistan mineralized area based on spectral analysis of ASTER data. *Remote Sens. Environ.* 104 (1): 74–87.
- [37]. Iwasaki, A. and Tonooka, H. (2005). Validation of Crosstalk correction algorithm for ASTER/SWIR. *IEEE T. Geosci. Remote.* 43 (12): 2747–2751.
- [38]. Matthew, M.W., Adler–Golden, S.M., Berk, A., Richtsmeier, S.C., Levine, R.Y., Bernstein, L.S., ..., and Ratkowski, A.J. (2000). Status of Atmospheric Correction Using a MODTRAN4– based Algorithm. In *Algorithms for Multispectral, Hyperspectral, and Ultraspectral Imagery*, 24 April 2000, Orlando, Florida (Florida: International Society for Optical Engineering). 4049: 199–207.
- [39]. Clark, R.N., Swayze, G.A., Wise, R., Livo, K.E., Hoefen, T., Kokaly, R.F. and Sutley, S.J. (2007). USGS digital spectral library splib06a. US geological survey, digital data series. 231 P.
- [40]. Rowan, L.C. and Mars, J.C. (2003). Lithologic mapping in the Mountain Pass, California, area using Advanced Spaceborne Thermal Emission and Reflection Radiometer (ASTER) data. *Remote Sens. Environ.* 84 (3): 350–366.
- [41]. Bedini, E., Van Der Meer, F. and Van Ruitenbeek, F. (2009). Use of HyMap imaging spectrometer data to map mineralogy in the Rodalquilar caldera, southeast Spain. *Int. J. Remote Sens.* 30 (2): 327–348.
- [42]. Green, A.A., Berman, M., Switzer, P. and Craig, M.D. (1988). A transformation for ordering multispectral data in terms of image quality with implications for noise removal. *IEEE T. Geosci. Remote.* 26 (1): 65–74.
- [43]. Boardman, J.W. (1998). Leveraging the high dimensionality of AVIRIS data for improved sub–pixel target unmixing and rejection of false positives: mixture tuned matched filtering. In *Summaries of the 7th Annual JPL Airborne Geoscience Workshop*, Pasadena, CA (Pasadena, CA: Jet Propulsion Laboratory). pp. 55–56.
- [44]. Congalton, R.G. (1991). A review of assessing the accuracy of classifications of remotely sensed data. *Remote Sens. Environ.* 37 (1): 35–46.

ارزیابی تأثیر استفاده از طیف‌های مرجع مختلف بر روی نتایج طبقه‌بندی SAM: رویکردی برای نقشه‌برداری دگرسانی گرمایی

مهدی هنرمند^{۱*}، حجت اله رنجبر^۲، هادی شهریار^۳ و فرزین ناصری^۱

۱- گروه اکولوژی، پژوهشگاه علوم و تکنولوژی پیشرفته و علوم محیطی، دانشگاه تحصیلات تکمیلی صنعتی و فناوری پیشرفته، کرمان، ایران

۲- گروه مهندسی معدن، دانشگاه شهید باهنر کرمان، ایران

۳- گروه مهندسی معدن، دانشگاه ولی عصر (عج) رفسنجان، ایران

ارسال ۲۰۱۸/۵/۱۱، پذیرش ۲۰۱۸/۶/۱۹

* نویسنده مسئول مکاتبات: mehonarmand167@yahoo.com

چکیده:

این تحقیق با هدف ارزیابی صحت طبقه‌بندی نقشه‌بردار زاویه طیفی (SAM) با استفاده از طیف‌های مرجع مختلف انجام شد. تصاویر رقومی تابش‌سنج بازتابی و گسیلش گرمایی فضاپرد پیشرفته (ASTER) در طبقه‌بندی به روش SAM برای نقشه‌برداری سنگ‌های دگرسان شده گرمایی، در کمان ماگمایی سنوزوئیک کرمان (KCMA) واقع در ایران مورد استفاده قرار گرفتند. منطقه مطالعاتی دربرگیرنده کانسارهای مس پورفیری مهمی همچون میدوک و چاه فیروزه است. گردآوری طیف‌های مرجع پس از پیش‌پردازش تصاویر VNIR/SWIR سنجنده ASTER در نظر گرفته شد. سه نوع طیف مرجع شامل طیف تصویر، کتابخانه طیفی USGS و طیف نمونه‌های صحرایی در الگوریتم SAM به کار گرفته شدند. راستی آزمایشی زمینی و مطالعات صحرایی شامل مطالعات مقاطع نازک، تجزیه پراش پرتوی ایکس (XRD) و طیف‌سنجی انعکاسی VNIR-SWIR برای صحت‌سنجی نتایج به انجام رسیدند. صحت طبقه‌بندی SAM به طور عددی با استفاده از یک ماتریس ابهام محاسبه شد. بهترین صحت روش SAM به میزان ۷۴/۰۱٪ با ضریب کاپای ۰/۶۵ با استفاده از طیف نمونه‌های صحرایی به عنوان طیف مرجع به دست آمد. افزون بر این، نتایج روش SAM با روش پالایش تطبیقی تنظیم شده آمیخته (MTMF) اعتبارسنجی شد. بررسی‌های صحرایی نشان دادند بیش از ۹۰٪ کانی‌زایی‌های مس شناخته شده درون نواحی دگرسانی بارزسازی شده قرار گرفته‌اند.

کلمات کلیدی: نقشه‌بردار زاویه طیفی، ASTER، دگرسانی گرمایی، کانسار مس پورفیری، کمان ماگمایی سنوزوئیک کرمان.